https://doi.org/10.2352/EI.2026.38.6.ISS-283

Circuit Flicker Noise Modeling for Pixels in Event-Based Vision Sensors

Daisuke Saito, Xiaozheng Mou, Menghan Guo, Dahai Zhou, Boyd Fowler;
OMNIVISION,Santa Clara,CA,USA

Abstract

Event-based vision sensors (EVS) are gaining interest in applications requiring low latency, high dynamic range, and energy-efficient imaging, such as image deblurring, object detection for autonomous vehicles, and AR/VR glasses. Unlike conventional frame-based sensors, their performance is highly sensitive to device-level noise processes, especially in low-light scenes. In previous work, we proposed a framework for pixel-wise parameter estimation for EVS characterization. We introduced a physics-based model and a shot noise model and validated them on a typical pixel setup. However, that model did not explicitly account for flicker noise, despite its being one of the major noise sources in modern CMOS technologies—a key factor behind pixel-to-pixel variability and spurious "noisy pixels," whose strength depends strongly on the technology.

In this paper, we introduce a dedicated flicker-noise component into the previously developed EVS simulator. We calibrated the circuit flicker noise model using circuit-level simulations and sensor measurements, achieving an error margin of less than 20%. The resulting model reproduces EVS circuit noise statistics and generates realistic synthetic event streams. The results indicated that flicker noise was larger than the value expected from SPICE simulation by a factor of five. Our work enables circuit-level trade-off studies and offers intuitive noise visualizations for both hardware designers and algorithm developers to assess algorithmic impact.

1. Introduction

Event-based Vision Sensors (EVS) detect changes in log intensity based on a predefined threshold and report them as asynchronous events with microsecond latency and high dynamic range [1, 2]. Their utility in robotics, augmented reality/virtual reality, and high-speed perception is affected by various noise sources, including device mismatch, fixed-pattern effects, thermal noise, shot noise, and flicker noise. Compared to conventional CMOS image sensors (CIS), which integrate photocurrent to obtain absolute intensity, EVS detects temporal contrast and outputs sparse asynchronous events. This enables low-latency operation and high dynamic range, but it also makes the system inherently sensitive to noise in the analog front-end.

In particular, noise events can substantially degrade image quality and impair downstream algorithm performance, especially in hybrid CIS+EVS systems that require synchronization and fusion for tasks such as deblurring and video interpolation [3]. Flicker noise is especially important in vision sensors because it induces slow threshold drift, leading to background activity and the emergence of “noisy pixels,” which in turn cause unexpected event generation. Flicker noise can vary by orders of magnitude depending on process technology and circuit design, making it challenging to isolate from other noise sources using sensor-level measurements alone.

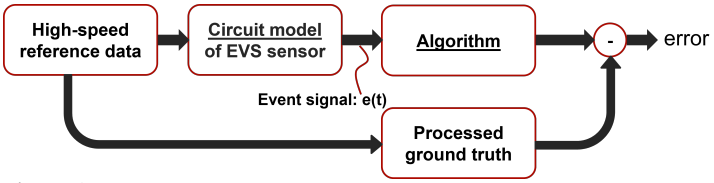

Figure 1: Pipeline of circuit design and algorithm evaluation using a unified EVS modeling framework with an EVS pixel model.

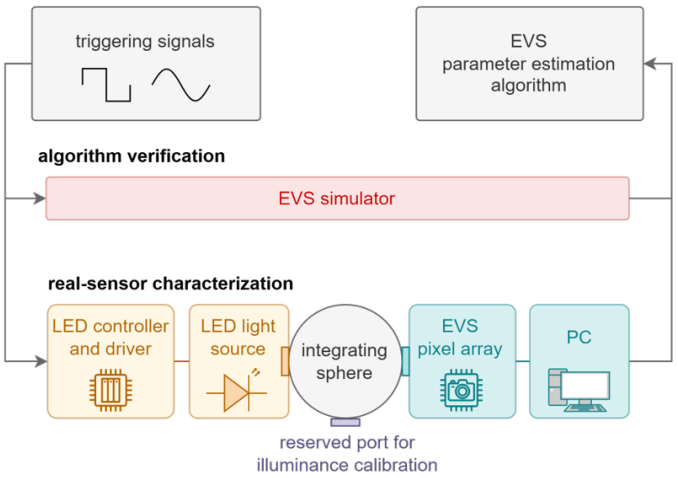

Figure 2: Parameter estimation formulated as an optimization problem to minimize measurement-prediction error [4].

In our previous work, shown in Fig. 1, we built the pipeline for circuit design and algorithm evaluation. The pixel-circuit model of the EVS sensor in the simulator generated synthetic event data from reference data captured with a high-speed camera. These event data could be used for algorithm development, while the reference data could be processed to obtain ground-truth data. In this way, the work bridged circuit design and algorithm development by enabling the evaluation of sensor-design trade-offs and the generation of reliable synthetic event data. For the EVS sensor model in the simulator, as shown in Fig. 2, we proposed an EVS pixel-wise joint parameter estimation method, including a shot noise model [4, 5]. This method coupled an ordinary differential equation-based latency model with an autoregressive (AR) Monte Carlo process. We validated this method by matching event firing-probability S-curves to analytically identified key pixel parameters. While

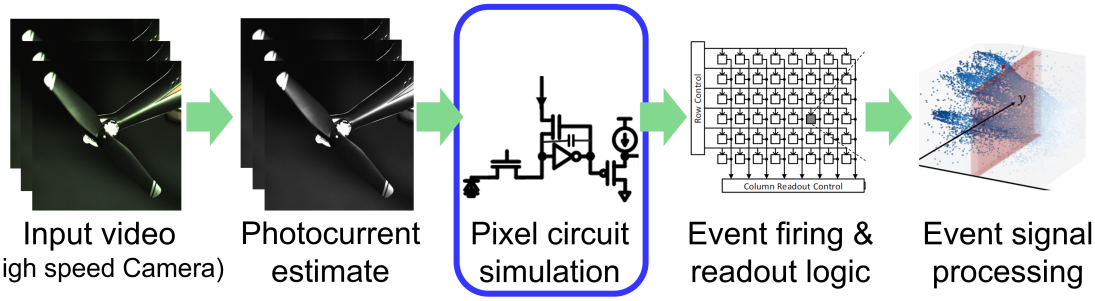

Figure 3: Physical sensor-model-based EVS simulator, including photocurrent estimation, pixel circuit simulation, and event generation [6].

the model successfully matched event firing probability under many conditions, it approximated noise as shot-noise dominated and did not explicitly model flicker noise. This limitation led to discrepancies between simulated and measured event statistics, particularly under low-light conditions, where low-frequency noise dominated. The goal of this work was to develop and validate a physics-based EVS pixel model that accounted for flicker noise in addition to shot noise. We introduced a flicker-noise into physical models into the previously developed EVS simulator (Sec. 2 and Sec. 3). We calibrated the circuit flicker noise model using circuit-level simulations and sensor measurements. This circuit flicker noise model generated realistic synthetic event streams and compared with the measurement results (Sec. 4).

2. Baseline Simulator and Evaluation Method

We use a previously developed physical sensor-model-based EVS simulator that models the entire signal chain, from input stimulus to event output [6]. Figure 3 shows the EVS simulator flow. The simulator takes high-speed video as input, estimates photocurrent, simulates pixel circuit behavior, and generates event streams through event firing and readout logic. One of the core components of the simulator is the "pixel circuit simulation." Figure 4 (a) illustrates a simplified schematic of the analog front end of an EVS pixel. The photodiode current, which includes dark current, is represented by $I_{PD} = I_{photo} + I_{dark}$, and is converted into a logarithmic voltage measured at node V_{FE}. The source follower M_{SF} decouples the EVS analog front-end circuit from a difference-detecting switched-capacitor amplifier with gain G. Subsequent comparators determine whether a temporal contrast beyond a predefined threshold has been detected. Figure 4 (b) shows the temporal contrast input measurement method [7, 8]. Figure 4 (c) illustrates that as the contrast input, defined as $C = [\Phi_2 - \Phi_1]/\Phi_1$, increases, there is a corresponding rise in the probability of event firing. The contrast level at which the firing probability reaches 50% is defined as the Nominal Contrast Threshold (NCT) [9]. This measure is important because it indicates the effective contrast threshold of a pixel under specific measurement conditions. Ideally, the transition from low to high firing probability is sharp around the NCT value. However, temporal noise introduces randomness in trigger probability, resulting in the characteristic "S-curve." The slope of the S-curve is crucial for pixel characterization. For S-curve characterization, it is preferable to select a small region of interest to isolate readout delay and uncertainty from pixel latency. It is evident that the NCT strongly depends on factors such as radiance, the time interval for pixel reset, the applied scene contrast step, and the overall observation time during which noise may exceed the contrast threshold. This suggests that the established metrics may not have full predictive value under varying operating conditions. Therefore, a model-based approach is necessary.

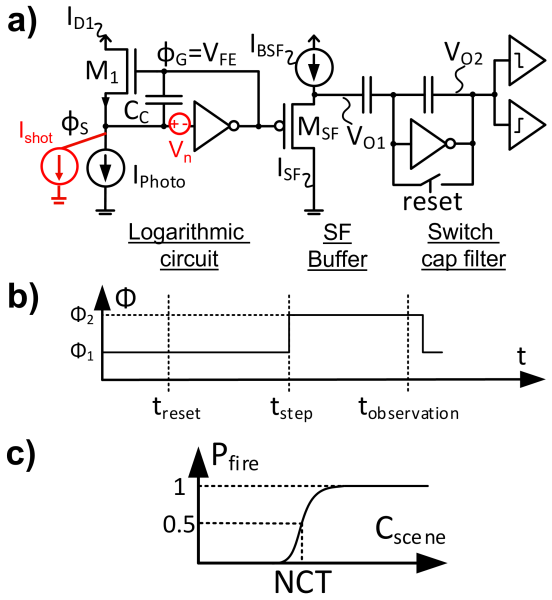

Figure 4: a) Analog EVS pixel circuit schematic, b) temporal contrast measurement timing diagram, and c) event firing probability "S-curve".

In the previous model, the EVS pixel was described using a combination of ordinary differential equations (ODEs) and an AR noise process. Shot noise was modeled as a stochastic process injected into the circuit nodes, and Monte Carlo simulations were used to generate noise realizations. The S-curve serves as a key evaluation metric, representing the probability of event firing as a function of input contrast. A mismatch in the slope of the S-curve directly reflects inaccuracies in the noise model. However, only shot noise was considered in this framework. As shown in Fig. 5, the simulated S-curve (event firing probability versus contrast) exhibits a steeper slope than the measured one, indicating missing noise contributions.

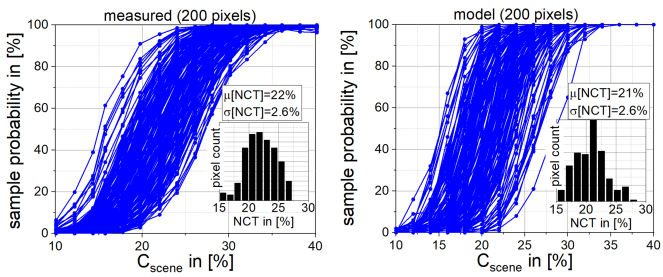

Figure 5: Comparison of measured pixel-level S-curves (left) and model predicted S-curves (right), [4].

3. Pixel Noise Modeling

3.1 Large-Signal Model

Assuming that all transistors operate in saturation and weak inversion, and that the inverting amplifier in the feedback loop of the logarithmic amplifier exhibits idealized affine-linear behavior, while neglecting its additional pole, we can model the large-signal response using simple ordinary differential equations [5]. The logarithmic amplifier follows:

$$\frac{\mathrm{d}\Delta V_{\mathrm{FE}}(t)}{\mathrm{d}t} + \frac{A \cdot I_{\mathrm{D1}}(t_0)}{[1+A]\cdot C_{\mathrm{C}}} \cdot \exp\left(\frac{\zeta + A}{A \cdot \zeta \cdot V_{\mathrm{T}}} \cdot \Delta V_{\mathrm{FE}}(t)\right) = \frac{A}{[1+A]\cdot C_{\mathrm{C}}} \cdot I_{\mathrm{PD}}, \quad (1)$$

where, ΔV_{FE} denotes the relative signal change at the output of the logarithmic amplifier with respect to the signal at the last sampled reference luminance level. Here, A is the open-loop gain of the inverting amplifier, I_{D1} is the current through the transistor whose source is connected to the photodiode and implements the linear-to-logarithmic conversion, I_{PD} is the photocurrent, C_{C} is the feedback capacitance between the input and output of the log-amplifier; ζ is the transistor subthreshold-slope parameter; and V_{T} is the thermal voltage.

The source-follower is designed to prevent kickback from the switched capacitor circuit that performs the difference detection. It is modeled as:

$$\frac{\mathrm{d}\Delta V_{\mathrm{O1}}(t)}{\mathrm{d}t} = \frac{1}{C_{\mathrm{LSF}}} \cdot \left[I_{\mathrm{BSF}} - I_{\mathrm{SF}}(t_0) \cdot \exp\left(\frac{\zeta \cdot \Delta V_{\mathrm{O1}}(t)}{\zeta \cdot V_{\mathrm{T}}} - \frac{\Delta V_{\mathrm{FE}}(t)}{\zeta \cdot V_{\mathrm{T}}}\right)\right], \quad (2)$$

where ΔV_{O1} is the relative output signal change, I_{SF} is the current through the source-follower transistor, I_{BSF} is its bias current, and C_{LSF} is the load seen by the source-follower.

It can be shown that the logarithmic amplifier has an analytical solution for a step-response in photocurrent $I_{\text{photo-0}} \rightarrow I_{\text{photo-1}}$:

$$\Delta v = \frac{\Delta V_{\mathrm{FE}}}{V_{\mathrm{T}} \cdot \frac{A\cdot\zeta}{\zeta+A}} = \ln\left(\frac{I_{\text{photo-1}}}{I_{\text{photo-0}}} \cdot \frac{1}{1 + C_{\mathrm{scene}} \cdot \exp[-[t-t_0]/\tau]}\right), \quad (3)$$

with the time-constant $\tau = \frac{1+A}{A} \cdot \frac{A\cdot\zeta}{\zeta+A} \cdot \frac{V_{\mathrm{T}}\cdot C_{\mathrm{C}}}{I_{\text{photo-1}}}$. Assuming that the bandwidth limitation of the log-amplifier is more significant than the source-follower, an analytical response can be found as:

$$\Delta V_{\mathrm{O1}}(t) \approx \frac{1}{\zeta} \cdot \Delta V_{\mathrm{FE}}(t) \quad (4)$$

3.2 Low-Light Noise Behavior

We introduce a dedicated flicker-noise component into the EVS pixel-noise model in addition to the existing shot-noise model. Accurate modeling of flicker noise, which is a low-frequency noise source, is especially critical under low-light conditions, because in this regime not only shot noise but also flicker noise becomes dominant. Figure 6 depicts the small-signal equivalent pixel circuits used to derive the noise model. Photon shot noise and pixel circuit noise, including both thermal noise and flicker noise are assumed to be injected as shown in Fig. 4 (a). The EVS analog front-end transfer function under low-light conditions is shown in Fig. 7. Figure 7 (a) is the transfer function for photon shot noise. As the light levels decrease, the photocurrent decreases, leading to a smaller transconductance ($g_{mG1} \propto \frac{I_{photo}}{V_T}$). Consequently, the system bandwidth shifts to lower frequencies ($p_d \propto \frac{g_{mG1}}{C_c}$), while the gain of low-frequency noise components increases, as indicated by $A_1 \propto \frac{1}{g_{mG1}}$. In addition to that, EVS pixels need to be binned to get sufficient photo current under low light conditions, resulting in the larger photo diode capacitance than no-binning pixel. This larger capacitance increases the pixel circuit noise gain of the transfer function, as indicated by $A_2 \propto \frac{C_{pd}}{C_c}$ in Figure 7 (b). As a result, flicker noise which is low frequency noise component, becomes dominant.

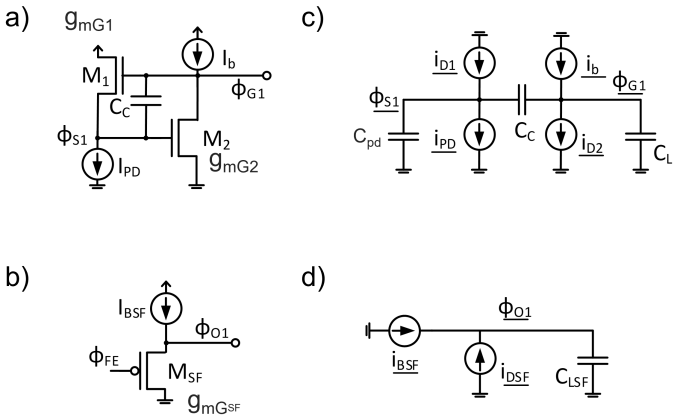

Figure 6: Simplified log-amplifier schematic (a) and source-follower schematic (b) and, with their respective small-signal circuits in (c) and (d), respectively.

3.3 Flicker-Noise Model

Noise is assumed to be a small-signal phenomenon. Figure 6 shows simplified schematics of the logarithmic amplifier in (a) and the source-follower in (b), and their small-signal equivalent representations are given in (c) and (d). Here, channel length modulation is ignored.

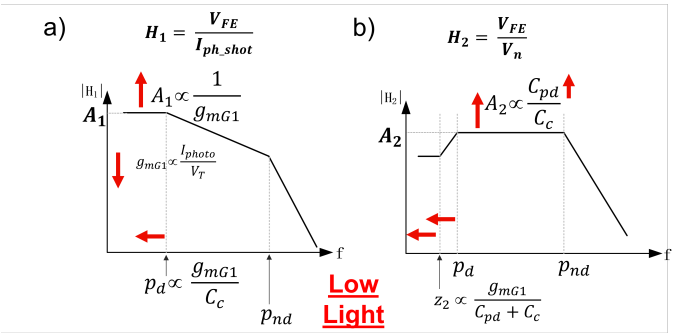

Figure 7: EVS analog front end transfer function at low light level for (a) photon shot noise and (b) circuit noise including both thermal noise and flicker noise.

For an NMOS transistor, $i_{\underline{D}}$ is given by:

$$\underline{i_D} = g_{mG} \cdot \underline{\varphi_G} + g_{mS} \cdot \underline{\varphi_S} \tag{5}$$

$$g_{mG} = \frac{\partial I_D}{\partial \varphi_G} = \frac{I_D}{\zeta \cdot V_T} \tag{6}$$

$$g_{mS} = \frac{\partial I_D}{\partial \varphi_S} = -\frac{I_D}{V_T} = -g_{mG} \cdot \zeta. \tag{7}$$

PMOS characteristics can be derived analogously.

We assume that $I_b \gg I_{photo}$ such that $g_{mG2} \gg g_{mG1}$. Using the dominant-pole approximation[1] , $\underline{\varphi_{G1}}$ in Fig. 6 (c) becomes:

$$\underline{\varphi_{G1}} = \frac{\underline{i_{PD}}}{g_{mG1}} \cdot \frac{1 - j\omega/z_1}{[1 + j\omega/p_{d1}] \cdot [1 + j\omega/p_{nd1}]} + \frac{\underline{i_b}}{g_{mG2}} \cdot \frac{1 + j\omega/z_2}{[1 + j\omega/p_{d2}] \cdot [1 + j\omega/p_{nd2}]}, \tag{8}$$

with the zeros $z_1 = \frac{g_{mG2}}{C_C}$ and $z_2 = \frac{g_{mG1} \cdot \zeta}{C_C + C_{pd}}$, dominant poles $p_{d1} = p_{d2} = \frac{g_{mG1}}{C_C}$ and non-dominant poles $p_{nd1} = p_{nd2} = \frac{g_{mG2}}{C_{pd} \cdot \frac{C_C + C_{pd} + C_L}{C_C}}$. We found that the dominant flicker-noise source was generated by the transistor in the inverting amplifier of the logarithmic circuit. We assumed that the transfer function of flicker noise was $H(s) = \frac{V_{FE}}{V_n}$ in Fig. 4 (a). Therefore, in Eq. 8, only the second transfer function is considered, since the first term became constant for the transfer function characteristics analysis of flicker noise. As $z_2 \ll p_{d2} \ll p_{nd2}$, the second transfer function first increases the gain between z_2 and p_{d2} and then decreases. Hence, p_{nd2} can be neglected, but z_2 cannot, since low-frequency noise is being modeled. The approximation yields:

$$\underline{\varphi_{G1}} = V_n \cdot \frac{1 + j\omega/z_2}{1 + j\omega/p_{d_2}} \tag{9}$$

$$H(s) = \frac{V_{FE}}{V_n} = \frac{1 + s/z_2}{1 + s/p_{d2}} \tag{10}$$

[1]Dominant-pole approximation expresses a transfer function by dominant p_d and non-dominant p_{nd} poles: $\frac{1}{1 + j\omega\alpha + (j\omega)^2 \cdot \beta} \approx \frac{1}{[1 + j\omega/p_{pd}] \cdot [1 + j\omega/p_d]}$. With $\frac{1}{[1 + j\omega/p_{pd}] \cdot [1 + j\omega/p_d]} \approx \frac{1}{1 + j\omega/p_d + (j\omega)^2/(p_{pd} \cdot p_d)}$, $p_d = 1/\alpha$ and $p_{pd} = \alpha/\beta$ result.

We use the McWhorter superposition of Lorentzians for the flicker noise model [10], which is well-behaved, stationary, ergodic, and easy to translate into variance. Flicker noise is modeled as a weighted sum of Lorentzian spectra, resulting in a $1/f$ power spectral density (PSD). For weak inversion operation in saturation the single-sided PSD is described as:

$$S_{I_D, I_D - flicker}(f) = \sum_{k=1}^{m} \frac{\alpha_k}{1 + (2\pi f \tau_k)^2} \tag{11}$$

Here, α_k denotes the coefficient used to form the $\frac{1}{f}$ frequency dependence of the flicker noise, and f_{τ_k} is the frequency parameter of each Lorentzian spectrum. Figure 8 illustrates the generated flicker-noise PSD in the blue plot. McWhorter's superposition of Lorentzians successfully modeled flicker noise which follows the expected trend of 10 dB per decade.

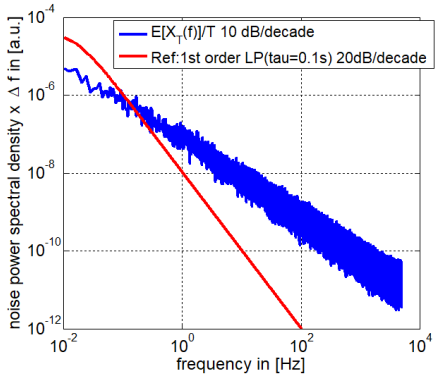

Figure 8: Power spectral density of flicker noise based on the McWhorter model.

Here, we consider the transfer characteristic, including the frequency dependence of flicker-noise. Since the flicker-noise PSD is described by a weighted summation of Lorentzians, and each weighted Lorentzians generates a transfer function given by:

$$H(s) \cdot h_{flicker_k}(s) = \frac{V_{fe}}{V_n} = \frac{1 + s/z_2}{1 + s/p_{d2}} \cdot \frac{2\sqrt{1/p_k}}{1 + s/p_k}$$

$$= 2\sqrt{1/p_k} \cdot \left(\frac{\frac{1/p_{d2} - 1/z_2}{1/p_{d2} - 1/p_k}}{1 + s/p_{d2}} + \frac{\frac{1/z_2 - 1/p_k}{1/p_{d2} - 1/p_k}}{1 + s/p_k}\right) \tag{12}$$

where, p_k is frequency in transfer characteristic of $h_{flicker_k}(s)$. The autocorrelation functions of noise sources at V_{FE} are:

$$R_{k\,FE,FE}(\Delta t) = K \cdot (2\sqrt{1/p_k})^2 \cdot \left(\frac{(\frac{1/p_{d2} - 1/z_2}{1/p_{d2} - 1/p_k})^2}{4(1/p_{d2})} \cdot e^{-\frac{|\Delta t|}{(1/p_{d2})}} + \frac{(\frac{1/z_2 - 1/p_k}{1/p_{d2} - 1/p_k})^2}{4(1/p_k)} \cdot e^{-\frac{|\Delta t|}{(1/p_k)}}\right) \tag{13}$$

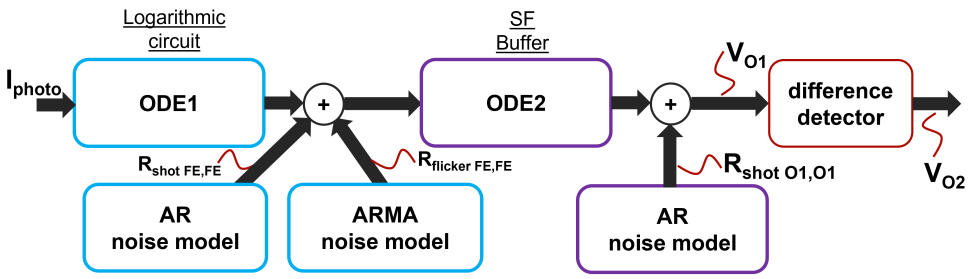

Figure 9: Schematic signal flow of the pixel model for small-signal flicker noise and shot noise, combined with large-signal deterministic behavior.

Shot noise is also modeled from our previous work based on Fig. 4 (a) to (d) as described in [5].

3.4 Autoregressive Moving-Average (ARMA) Noise Model

Figure 9 illustrates the signal flow used in the presented EVS model. The photodiode current $I_{\text{PD}} = I_{\text{photo}} + I_{\text{dark}}$ is propagated to V_{FE} using the ODE1 model of a logarithmic circuit (in Eq. 1) solved using Forward-Euler integration. Flicker noise is added in a way that matches the autocorrelation function in Eq. 13. The superposition of signal and noise is then fed into the ODE2 model of the source-follower buffer. As shown in [5], shot noise is also added to the signal generated by the ODE1 model of a logarithmic circuit, followed by the buffer-noise contribution in ODE2 model, such that the resulting autocorrelation function matches the target. The final result is then used to drive the difference detecting circuit which is also modeled by a simple differential equation in order to represent signal-dependent leak events and the high-pass-filter characteristic proposed in [11].

By construction, the flicker noise model for each weighted Lorentzian in Eq. 13 describes a second-order zero-pole system. Using Forward-Euler integration, the response x_k of such a system to noise f_k becomes a second-order autoregressive moving average (ARMA) model [12]:

$$\begin{aligned} & x_k(n) \\ & = (2 - \frac{\Delta t^2}{\tau_p \tau_k} \frac{(\tau_p + \tau_k)}{\Delta t}) \cdot x_k(n-1) + \\ & (\frac{\Delta t^2}{\tau_p \tau_k} \frac{(\tau_p + \tau_k)}{\Delta t} - \frac{\Delta t^2}{\tau_p \tau_k} - 1) \cdot x_k(n-2) + \\ & f_k(n) + (\frac{\Delta t}{\tau_z} - 1) \cdot f_k(n-1) \\ & = \Phi_{2,1} \cdot x_k(n-1) + \Phi_{2,2} \cdot x_k(n-2) + \\ & \qquad f_k(n) + \theta_{1,1} \cdot f_k(n-1) \end{aligned} \tag{14}$$

Here, τ_p, τ_z, and τ_k are the time constants associated with the pole, zero, and Lorentzian component, respectively, and Δt is the Forward-Euler time-step. A white Gaussian-noise process, $e(n)$, with $e(n) \sim \mathcal{N}(0, \sigma)$, is generated using a random-number generator. This noise process is then used to generate $f_k(n-1), f_k(n) \sim \mathcal{N}\left(0, \sigma \cdot \frac{\Delta t^2}{\tau_p \tau_k} \frac{\tau_z}{\Delta t}\right)$. By choosing $E[x_k(0)] = 0$, it can be shown that $x_k(n)$ is wide-sense stationary. A sum of the x_k terms then yields the final flicker-noise output X.

$$\Rightarrow E[x_k(n)] = 0 \tag{15}$$

$$\Rightarrow \text{var}[x_k] = \sigma \cdot \frac{(1+\Phi_{k2,2})[(1-\Phi_{k2,2})^2 - \Phi_{k2,1}^2]}{[2\theta_{k1,1}\Phi_{k2,1} + (1-\Phi_{k2,2})(1+\theta_{k1,1}^2)]} \tag{16}$$

$$x(n) = \sum_{k=1}^{m} x_k(n) \tag{17}$$

$$coef = \sum_{k=1}^{m} \frac{1}{(2\sqrt{\tau_k})} \tag{18}$$

$$X(n) = \frac{x(n)}{coef} \tag{19}$$

We can derive $R_{kx,x}(1), R_{kx,x}(2), ..., R_{kx,x}(n)$ from Eq. 14. Furthermore, the autocorrelation function of such an ARMA process $R_{kx,x\text{-a.r.}}$ converges to the time-continuous form of $R_{kx,x\text{-t.c.}}$ modeling white noise in a second-order zero-pole system. Rearranging Eq. 16 for σ as a function of the desired σ_{x_k} and τ (cf. Eq. 13 and the step size Δt yields physical noise behavior with the desired magnitude and bandwidth. This means that we obtain $\Phi_{k2,1}$, $\Phi_{k2,2}$, and $\theta_{k1,1}$ with analytically modeled noise variance. In our event-vision simulator, these autocorrelation functions were used to create Monte Carlo trials using ARMA noise model. The blue plot in Fig. 10 shows the simulated noise PSD generated by the EVS pixel-circuit noise model, which shows expected noise PSD.

4. Experimental Results

We introduced the flicker-noise model into the EVS simulator alongside the shot noise model. First, the circuit noise output was modeled using SPICE simulation. Then, we calibrated this noise level to adjust the pixel-level EVS noise associated with the device and technology by using measured events. This two-step calibration ensured consistency between circuit-level simulations and system-level measurements.

The flicker-noise variance in the EVS circuit at V_{O2} in Fig. 4 (a) was extracted from the simulated circuit output and compared against SPICE simulations. As shown in Fig. 11, the simulated flicker noise closely matched the SPICE results within 20 % across various illumination levels. The flicker noise increased as

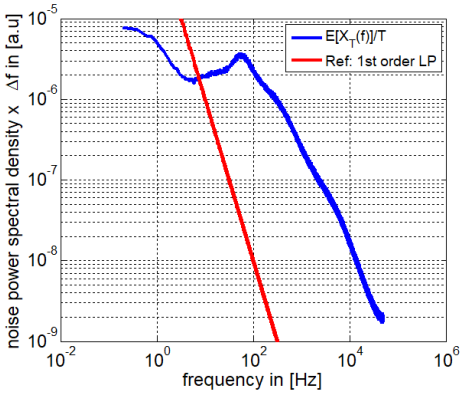

Figure 10: Power spectral density of flicker noise at the EVS pixel circuit output V_{O1} in Fig. 4 (a).

the illuminance decreased because the dominant pole shifted towards lower frequencies, resulting in a higher gain in the low-frequency region, as shown in Fig. 7 (b).

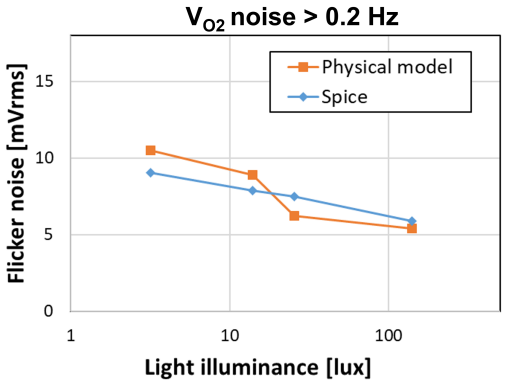

Figure 11: EVS pixel-circuit output-voltage variance at V_{O2} in Fig. 4 (a) predicted by the developed noise model and by SPICE simulation at low-light illumination from 3 to 140 lux.

Using the noise model calibrated against SPICE results, we simulated event probabilities and compared them with measured data. Figure 12 shows the measured and simulated event-probability S-curves. The events were simulated at a 14-lux illuminance level. This was selected from 10000 pixels' output to eliminate the impact of contrast input variation elements other than flicker noise. The curve shown in blue was generated from shot noise and the curve shown in light pink is generated SPICE-calibrated flicker noise. These two curves did not match the measured results. In contrast, good agreement with the measured results was obtained only when the flicker-noise level was increased to 33 and 48 mVrms, as shown by the purple and pink curves, respectively. This indicated that the actual flicker noise was approximately five times larger than that predicted by SPICE simulation. This difference is also clearly reflected in the noise-event maps at low contrast levels in Fig. 12: the map corresponding to 48 mVrms flicker noise (pink plot) exhibits higher noise-event activity than that for 9 mVrms flicker noise (light pink plot) at 0.22 input contrast. These results demonstrated the strong impact of flicker noise on event generation and highlighted the importance of sensor-level noise modeling and calibration, especially in low light conditions.

5. Conclusion

This work provides an EVS pixel model that (i) explicitly incorporates flicker noise with SPICE-tied parameters, (ii) is calibrated jointly to device-level simulations and sensor-level statistics, and (iii) synthesizes event streams that capture noisy-pixel behavior. Relative to our previous shot-noise model, we:

1. introduced a dedicated, calibrated flicker-noise component;
2. performed a two-step calibration using both SPICE and measurement data to determine the flicker-noise level; and
3. enabled realistic synthetic event data to support design trade-off studies and future algorithm evaluation.

The results demonstrate that flicker noise plays a critical role in EVS performance, particularly in low-light conditions, and

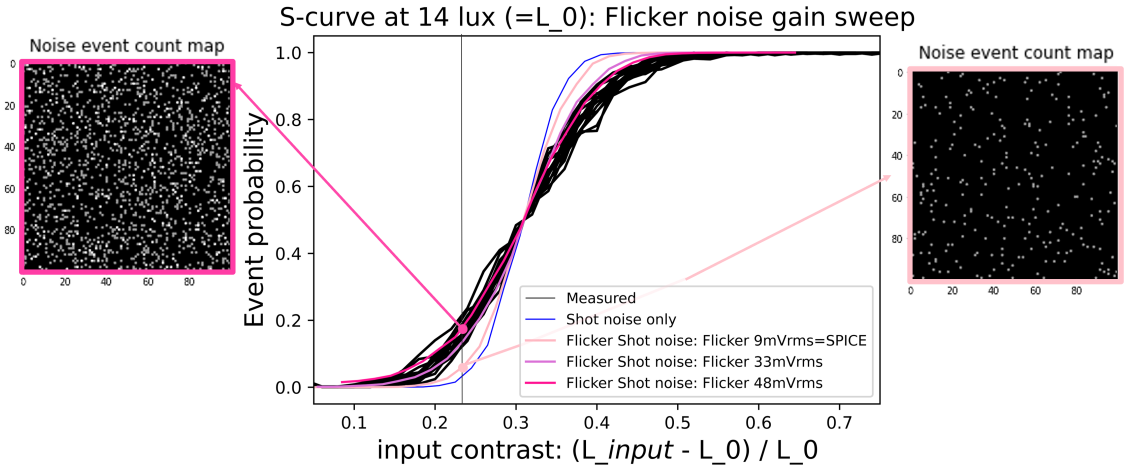

Figure 12: Measured and simulated event probability S-curves with shot noise and flicker noise at 14-lux illumination as a function of input contrast. The measured data are compared against a simulation including only shot noise and simulations incorporating varying levels of flicker noise from 9 to 48 mVrms. Noise event count maps are shown for two flicker noise cases: 9 mVrms (SPICE-calibrated flicker noise) and 48 mVrms at 0.22 input contrast.

must be accurately modeled for both circuit design and algorithm evaluation. Exploration of circuit parameters and algorithmic impact, including denoising, tracking, and feature stability, is left for future work.

References

[1] G. Gallego, T. Delbruck, G. Orchard, C. Bartolozzi, B. Taba, A. Censi, S. Leutenegger, A. Davidson, J. Conradt, K. Daniilidis, and D. Scaramuzza, "Event-based vision: A survey," in IEEE Transactions on Pattern Analysis and Machine Intelligence, 2020.

[2] P. Lichtensteiner and T. Delbruck, "A 64x64 AER logarithmic temporal derivative silicon retina," Research in Microelectronics and Electronics, 2005 PhD, 2005, pp. 202-205

[3] D. Saito, et al., "Building end-to-end deblur image quality evaluation simulation for Hybrid-EVS-CIS sensor images", Electronic Imaging, 2025, pp 240–1 - 240-7, https://doi.org/10.2352/EI.2025.37.9.IQSP-240.

[4] X. Mou, R. Jiang, W. Zhang, M. Guo, B. Mu, A. Suess, "Joint Parameter Estimation for Event-Based Vision Sensor Characterization" in Electronic Imaging, 2024, pp 289-1 - 289-5, https://doi.org/10.2352/EI.2024.36.7.ISS-289

[5] A. Suess, M. Guo, R. Jiang, X. Mou, Q. Huang, W. Yang, S. Chen, "Physical modelling and parameter extraction for event based vision sensors", in Proc. IISS Int. Image Sensor Workshop (IISW), pp. R5.5, 2023.

[6] X. Mou, K. Feng, A. Yi, S. Wang, H. Chen, X. Hu, M. Guo, S. Chen, A. Suess, "Accurate event simulation using high-speed video," in Proc. IST Int'l. Symp. on Electronic Imaging: Imaging Sensors and Systems, 2022, pp 242-1 - 242-6, https://doi.org/10.2352/EI.2022.34.7.ISS-242.

[7] C. Posch and D. Matolin, "Sensitivity and uniformity of a 0.18 m CMOS temporal contrast pixel array," 2011 IEEE International Symposium on Circuits and Systems (ISCAS), Rio de Janeiro, Brazil, 2011, pp. 1572-1575, doi: 10.1109/ISCAS.2011.5937812.

[8] B. McReynolds, R. Graca, and T. Delbruck, "Experimental methods to predict dynamic vision sensor event camera performance," Opt. Eng., vol. 61, no. 7, p. 074103, Jul. 2022, doi: 10.1117/1.OE.61.7.074103.

[9] T. Finateu, A. Niwa, D. Matolin, K. Tsuchimoto, A. Mascheroni, E.Reynaud, P. Mostafalu, F. Brady, L. Chotard, F. LeGoff, H. Takahashi, H. Wakabayashi, Y. Oike and C. Posch, "A 1280x720 Back-Illuminated Stacked Temporal Contrast Event-Based Vision Sensor with 4.86um Pixels, 1.066GEPS Readout, Programmable Event-Rate Controller and Compressive Data-Formatting Pipeline," in IEEE International Solid-State Circuits Conference, 2020.

[10] L. K. J.Vandamme, "On the origin of 1/f noise in MOSFETs", Fluctuation and Noise Letters, 2007, 07:03, L321-L33, https://doi.org/10.1142/S0219477507003970

[11] M. Guo, S. Chen, Z. Gao, W. Yang, P. Bartkovjak, Q. Qin, X. Hu, D. Zhou, Q. Huang, M. Uchiyama, Y. Kudo, S. Fukuoka, C. Xu, H. Ebihara, X. Wang, P. Jiang, B. Jiang, B. Mu, H. Chen, J. Yang, T.J. Dai, A. Suess, "A three-wafer-stacked hybrid 15-MPixel CIS + 1-MPixel EVS With 4.6-GEvent/s readout, in-pixel TDC, and on-chip ISP and ESP function", in IEEE Journal of Solid-State Circuits, vol. 58, no. 11, pp. 2955-2964, Nov. 2023.

[12] K. S. Shanmugan and A. M. Breiphol, Random Signals, Wiley, July 1988.

Author Biography

Daisuke Saito received his M.E. degree in applied physics from Tsukuba University, Tsukuba, Japan. He is currently Sr. Staff Image Sensor Technology Engineer in the CTO Office at OmniVision Technologies, Inc. focusing on event vision-based sensor systems simulation and edge AI sensors.

JOIN US AT THE NEXT EI!

electronic IMAGING

Imaging across applications . . . Where industry and academia meet!

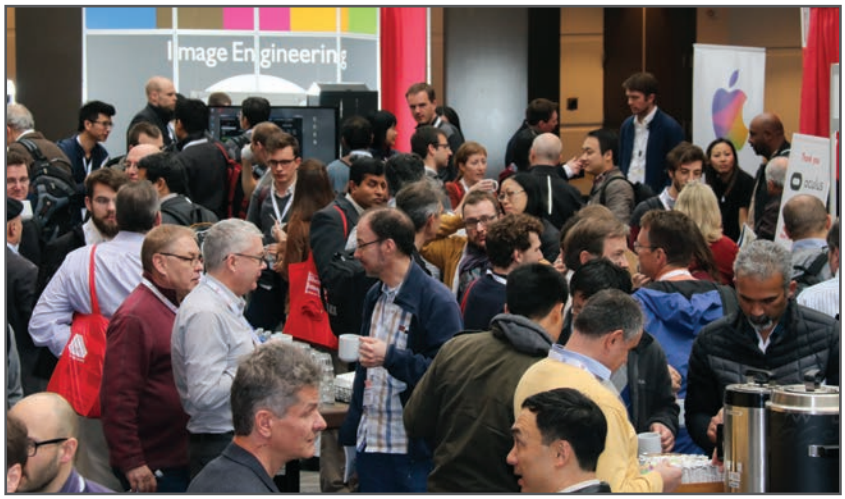

• SHORT COURSES • EXHIBITS • DEMONSTRATION SESSION • PLENARY TALKS •
• INTERACTIVE PAPER SESSION • SPECIAL EVENTS • TECHNICAL SESSIONS •

www.electronicimaging.org

ADVANCING IMAGING SCIENCE 75 1947 IS&T 2022 imaging.org